Journal of Applied Physics

Thermographic detection of internal defects using 2D photothermal super resolution reconstruction with sequential laser heating

Cite as: J. Appl. Phys. **131**, 185107 (2022); https://doi.org/10.1063/5.0088102
Submitted: 13 February 2022 • Accepted: 24 April 2022 • Published Online: 10 May 2022

J. Lecompagnon, S. Ahmadi, P. Hirsch, et al.

Journal of Applied Physics ARTICLE scitation.org/journal/jap

Thermographic detection of internal defects using 2D photothermal super resolution reconstruction with sequential laser heating

Cite as: J. Appl. Phys. **131**, 185107 (2022); doi: 10.1063/5.0088102
Submitted: 13 February 2022 · Accepted: 24 April 2022 ·
Published Online: 10 May 2022

J. Lecompagnon,[1,a)] S. Ahmadi,[1,b)] P. Hirsch,[1,b)] C. Rupprecht,[2] and M. Ziegler[1,b)]

AFFILIATIONS

[1]Bundesanstalt für Materialforschung und -prüfung (BAM), 12200 Berlin, Germany
[2]Technische Universität Berlin, 10623 Berlin, Germany

Note: This paper is part of the Special Topic on Non-Invasive and Non-Destructive Methods and Applications Part I â Festschrift.
[a)]**Author to whom correspondence should be addressed:** julien.lecompagnon@bam.de.
URL: https://www.bam.de/thermography
[b)]**URL:** https://www.bam.de/thermography

ABSTRACT

Thermographic photothermal super resolution reconstruction enables the resolution of internal defects/inhomogeneities below the classical limit, which is governed by the diffusion properties of thermal wave propagation. Based on a combination of the application of special sampling strategies and a subsequent numerical optimization step in post-processing, thermographic super resolution has already proven to be superior to standard thermographic methods in the detection of one-dimensional defect/inhomogeneity structures. In our work, we report an extension of the capabilities of the method for efficient detection and resolution of defect cross sections with fully two-dimensional structured laser-based heating. The reconstruction is carried out using one of two different algorithms that are proposed within this work. Both algorithms utilize the combination of several coherent measurements using convex optimization and exploit the sparse nature of defects/inhomogeneities as is typical for most nondestructive testing scenarios. Finally, the performance of each algorithm is rated on reconstruction quality and algorithmic complexity. The presented experimental approach is based on repeated spatially structured heating by a high power laser. As a result, a two-dimensional sparse defect/inhomogeneity map can be obtained. In addition, the obtained results are compared with those of conventional thermographic inspection methods that make use of homogeneous illumination. Due to the sparse nature of the reconstructed defect/inhomogeneity map, this comparison is performed qualitatively.

I. INTRODUCTION

One of the main factors that govern the resolution limit of thermographic nondestructive testing methods is the diffusive nature of heat conduction in solids. This has an especially severe impact on resolving defect/inhomogeneity structures that lie deep below the surface of the object under test (OuT). As a general rule, using well-established conventional thermographic testing methods, defects can only be fully resolved as long as their lateral extension is as large as they lie deep within the OuT. With the application of photothermal super resolution (SR) reconstruction techniques, it has already been proven that this limit can be overcome.

Super resolution imaging techniques have been successfully applied in several fields where there are resolution barriers to overcome. While geometrical super resolution techniques enhance the spatial resolution of modern detectors to a sub-pixel accuracy,[1,2] optical super resolution techniques allow us to overcome the classical Abbe diffraction limit of optical imaging systems.[3,4] However, currently established photothermal super resolution reconstruction methods within the field of active thermographic materials testing are restricted to the reconstruction of one-dimensional defect structures[5–7] or only approximate two-dimensional super resolution by combining several one-dimensional illumination patterns.[8]

Furthermore, in this context, it should be noted that in contrast to the aforementioned methods relying on the spatially structured heating of the OuT, there also exist reconstruction methods working with temporally structured illumination, which allow for a three-dimensional reconstruction of internal structures while also trying to eliminate thermal diffusion effects.[9,10]

Within this work, we expand the experimental approach behind laser-based photothermal SR reconstruction toward the detection of two-dimensional defects. This experimental approach is characterized by taking multiple independent measurements for a set of equidistantly distributed positions where the OuT is heated using a single round laser spot with a high power laser. For each of those illuminations, an independent measurement of the temperature response of the OuT is recorded with an infrared camera. In order to then reconstruct the internal defect/inhomogeneity pattern from the acquired set of independent measurements and gaining true two-dimensional information about the defect shape stripped from the blurring-effects of thermal diffusion, two different numerical methods for inverting the underlying severely ill-posed inverse problem are proposed. Subsequently, both methods are experimentally validated on a purpose-made additively manufactured sample with internal defect structures suitable to benchmark the resolution capabilities of each method.

II. MOTIVATION ON PHOTOTHERMAL SUPER RESOLUTION RECONSTRUCTION

The temporal progression of the front surface ($z = 0$) temperature T_{meas} of an OuT exposed to a localized external heat flux Q can be modeled as the sum of the initial temperature distribution on the OuT front surface at $t = 0\,\text{s}$ and the two-dimensional spatial convolution (denoted as $*_{x,y}$) of the thermal point spread function (PSF) Φ_{PSF} and a heat source distribution a,

$$T_{\text{meas}}(x, y, z = 0, t) = T_0(x, y) + \Phi_{\text{PSF}}(x, y, t) *_{x,y} a(x, y). \quad (1)$$

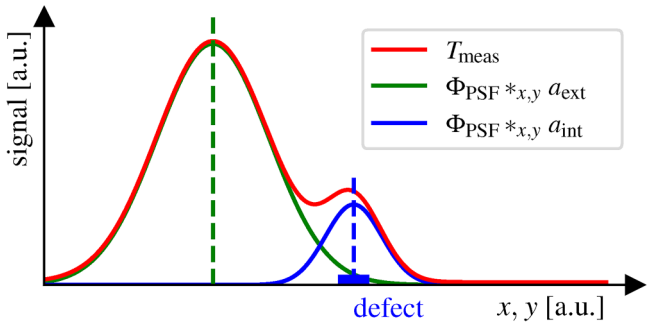

FIG. 1. Visualization of the components of the heat source distribution a: the measured temperature data T_{meas} can be modeled according to Eq. (1) as the sum of the external heat source distribution a_{ext}—the external photothermal heating—and the internal apparent heat source distribution a_{int}—the temperature deviations due to defects/inhomogeneities—convolved with the thermal PSF encoding the physics of heat conduction as well as the material parameters and geometry according to Eqs. (1) and (5). a_{ext} and a_{int} are additionally shown as dashed lines.

The thermal PSF resembles the kernel function in Green's-function like representation of the thermal diffusion differential equation. The PSF can be calculated analytically for the special case of a defect-free thin plate with thickness L as follows:[6,11]

$$\Phi_{\text{PSF}}(x, y, t) = \left(\frac{2\,\hat{Q}}{c_p \rho (4\pi\alpha t)^{n_{\text{dim}}/2}} \times e^{-\frac{(x-\bar{x})^2+(y-\bar{y})^2}{4\alpha t}} \times \sum_{n=-\infty}^{\infty} R^{2n+1}\, e^{-\frac{(2nL)^2}{4\alpha t}} \right) *_t I_t(t), \quad (2)$$

where

c_p is the specific heat capacity,
ρ is the bulk density,
α is the thermal diffusivity,
n_{dim} is the dimensionality of the heat flow:
  point-wise excitation: $n_{\text{dim}} := 3$,
  line-wise excitation: $n_{\text{dim}} := 2$,
  full-surface excitation: $n_{\text{dim}} := 1$,
$(\bar{x}, \bar{y})$ is the coordinate centroid of the excitation area,
R is the thermal wave reflection coefficient (for typical metals $R \approx 1$),
$*_t$ denotes convolution in time,
$\hat{Q}$ is the amplitude of the external heat flux Q, and
I_t is the temporal structure of Q.

For the derivation of Eq. (2), it is assumed that the external heat flux Q can be separated into its temporal structure given by I_t and its spatial structure $I_{x,y} *_{x,y} a_{\text{ext}}$ according to Eq. (3),

$$Q(x, y, t) = \hat{Q} \times I_{x,y}(x, y) *_{x,y} a_{\text{ext}}(x, y) *_t I_t(t). \quad (3)$$

Typically, I_t with $I_t(t) \in [0, 1]$ is a boxcar function with an active interval from $t \in [0, t_{\text{pulse}}]$, while $I_{x,y}(x, y) \in [0, 1]$ encodes the intensity distribution of the external photothermal heating and a_{ext} constitutes a distribution of Dirac delta impulses δ_i with a unit impulse at each excitation position,

$$a_{\text{ext}}(x, y) = \sum_i \delta_i(x_i, y_i). \quad (4)$$

While the temporal structure of the external heat flux is already considered within the PSF, the spatial structure is incorporated into the heat source distribution a, which is defined as follows:

$$a(x, y) = I_{x,y}(x, y) *_{x,y} (a_{\text{ext}}(x, y) + a_{\text{int}}(x, y)). \quad (5)$$

Here, the additional term a_{int} represents the spatial distribution of the internal "apparent" heat sources. In typical OuTs, even though there are no active internal heat sources present, the fact that regions with internal defects/inhomogeneities show up as higher temperature regions in T_{meas} lets them appear in the data as if they were independent heat sources (see Fig. 1). This is due to the fact that they impede the local heat flow at their respective positions. It should be noted that there exist also scenarios in which defective regions show a lower temperature for which $a_{\text{int}}(x, y)$ is

negative (apparent heat sinks). This is, for example, the case if the OuT includes inhomogeneities with a higher thermal effusivity than its bulk material. Both variants are equally covered by the presented modeling approach.

Therefore, if the heat source distribution a can be reconstructed for the OuT, then, in turn, also the defect/inhomogeneity structure of the OuT is known, which, in general, makes the reconstruction of a from Eq. (1) the overall goal of photothermal SR reconstruction. a_{int} can be described as a Dirac delta pulse distribution as follows:

$$a_{\mathrm{int}}(x, y) = \sum_i \zeta_i \times \delta(x_i, y_i), \tag{6}$$

where $\zeta_i \in [0, 1[$ serve as numerical weights in order to incorporate different defect signal strengths. These weights originate from the model assumption that all defects/inhomogeneities viewed as apparent heat sources feature the same PSF as the external heating but depending on their cross section and depth attenuated by the factor ζ_i. Since ζ_i cannot be easily separated from a_{int} within this modeling approach, by reconstructing the heat source distribution a and, therefore, a_{int}, no information about the defect cross section in the depth plane can be gained. a_{int}, therefore, only contains the in-plane information on the cross sections of the contained defects/inhomogeneities.

In order to solve the ill-posed problem as stated in Eq. (1) for the heat source distribution a, n_m measurements with $m \in \{1, \ldots, n_m\}$ are performed. For each measurement m, the photothermal heating pattern a_{ext} is varied, leading to a system of n_m equations to be solved simultaneously,

$$\Phi_{\mathrm{PSF}}(x, y, t) *_{x,y} a^m(x, y) = T^m_{\mathrm{diff}}(x, y, t), \tag{7}$$

with $T^m_{\mathrm{diff}}(x, y, t) = T^m_{\mathrm{meas}}(x, y, t) - T^m_0(x, y)$.

Even though the external component a_{ext} from Eq. (5) is in principle known as prior information, it was shown to be beneficial to also simultaneously reconstruct the external component a_{ext} besides a_{int}, leading to a blind reconstruction. If conversely a non-blind reconstruction approach is chosen, it is critical that the position and intensity profile of the external heating for each measurement is precisely known in order to not introduce reconstruction artifacts. In contrast, for a blind reconstruction, this requirement does not apply, reducing the overall experimental complexity. However, in order to make it possible to separate a_{ext} and a_{int} without artifacts in a blind reconstruction context, it must hold true that the sum of the external excitation over all measurements is constant as demanded by Eq. (8),

$$I_{x,y}(x, y) *_{x,y} \sum_{m=1}^{n_m} a^m_{\mathrm{ext}}(x, y) \approx const. \tag{8}$$

This condition is based on the fact that it can otherwise not be differentiated if a deviation from the mean is caused by an interference of a defect/inhomogeneity at that location or if it is caused by the non-uniformity of the sum of the external excitation.

Furthermore, to decrease the computational complexity, it is advantageous to eliminate the time dependency of Eq. (7) by only considering a single time step t_{eval}. When choosing a suitable time step, several factors have to be considered. In order to minimize measurement artifacts from the photothermal heating, a time step during the cooling phase $t_{\mathrm{eval}} > t_{\mathrm{pulse}}$ should be chosen. Due to the exponential nature of the cooling process, an early t_{eval} leads to higher SNR. Additionally, the thermal diffusion length of the thermal wave $L_{\mathrm{diff}} \propto t^{1/2}$ increases with time with the thermal diffusivity α of the bulk material acting as the proportionality constant,

$$L_{\mathrm{diff}}(t) = \sqrt{\alpha \times t}. \tag{9}$$

Since photothermal SR is only able to gain in-plane information of the contained defects/inhomogeneities, only the planar projection of the defect/inhomogeneity distribution within the testing volume spanned by the region of interest (ROI) and L_{diff} can be reconstructed. Therefore, choosing t_{eval} is a balance act between achieving sufficient SNR and maximum detection depth for internal defects as is emphasized by Fig. 2.

III. EXPANDING TO 2D-RECONSTRUCTION

Currently, well-established laser-based photothermal SR reconstruction methodology is restricted to reconstruction of defects along a single spatial dimension.[6,12] Here, the OuT is heated using line shape laser spots or patterns consisting of several laser lines either by scanning continuously over the ROI or by stepwise scanning. Even though in this way only defects that vary only in a single dimension can be detected, the method has proven to highly increase the resolution limit of thermographic testing. One factor of its success is based on the fact that one of the spatial dimensions can be collapsed by summation leading to a dramatic increase in SNR since all measured data in this collapsed dimension are redundant, which greatly reduces the measurement noise, which is not possible for typical two-dimensional defects.

Other approaches on achieving two-dimensional super resolution have been based on using movable slit-masks in conjunction with photothermal heating with the use of flashlamps. Here, the slit mask needs to not only be moved but also rotated to gain super resolution in the second dimension and the information gain about the second spatial dimension is discretized to the different rotation angles of the slit mask.[8] In order to expand the method to a two-dimensional reconstruction approach and to be sensitive in both spatial dimensions, a different heating strategy needs to be chosen.

If instead of scanning the OuT with laser lines a sequential point-wise scanning approach is used, where the sample is iteratively scanned on an equally-spaced grid by a single laser spot, 2D-super resolution can be achieved. In this scenario, $I_{x,y}$ can be modeled as a top-hat round laser spot with a diameter of d_{spot}. An equal spacing between all neighboring measurement positions can be achieved by arranging all measurements on a grid consisting of equilateral triangles of side length r_d (cf. Fig. 3). A square ROI with area $A_{\mathrm{ROI,2D}}$ and side length $L_{\mathrm{ROI,1D}}$ can, therefore, be covered by approximately $n_{m,2D} \approx \sqrt{3}/2 \times A_{\mathrm{ROI,2D}}/r_d^2$ independent

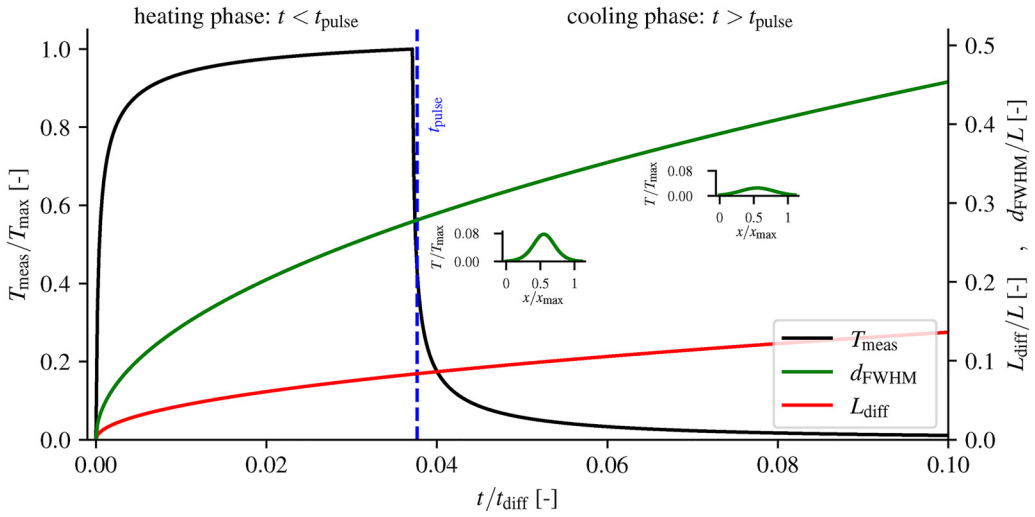

FIG. 2. Selection of t_{eval}: for eliminating the time dimension, the reconstruction is only performed for a single time step t_{eval}. This time step has to be chosen carefully with respect to the temperature signal strength (black line) for best SNR, the thermal diffusion length (red line), and the homogeneity requirement in conjunction with the measurement density governed by r_d, which is influenced by the width d_{FWHM} of the thermal PSF Φ_{PSF} (green line). The inset figures show the spatial extent of Φ_{PSF} at $t/t_{diff} = 0.045$ and 0.065, respectively. All shown graphs are normalized with the maximum temperature $T_{max} = \max(T_{meas})$ or the OuT thickness L and are plotted against the diffusion time $t_{diff} = L^2/\alpha$ to exclude the dependency on material properties and geometry.

measurements:

$$\frac{n_{m,2D}}{n_{m,1D}} \approx \frac{\sqrt{3} \times A_{ROI,2D}}{2 \times L_{ROI,1D} \times r_d} \tag{10}$$

$$\rightarrow \; n_{m,2D} \approx \frac{\sqrt{3}}{2} \times {n_{m,1D}}^2. \tag{11}$$

In order to achieve sufficient uniformity according to Eq. (8), r_d has to be chosen sufficiently small compared to the spatial full width at half maximum (FWHM) extension d_{FWHM} of the PSF, which has a direct effect on the amounts of independent measurements needed to cover the whole ROI. If for a reconstruction along a single dimension $n_{m,1D} = 200$ measurements are to be taken, for a 2D-reconstruction, now $n_{m,2D} \approx 34\,800$ measurements are necessary to achieve a similar resolution for a fixed spacing of measurements r_d.

The FWHM spot diameter $d_{FWHM}(t)$ for a PSF with $n_{dim} = 2$ is given by the following term considering the standard deviation $\sigma(t) = \sqrt{2\alpha \times t}$ of the PSF,

$$d_{FWHM}(t) = 4\sqrt{\ln(2)\alpha \times t}. \tag{12}$$

Here, the time dependency can be exploited such that choosing a late-enough t_{eval} will lead to a larger d_{FWHM} and, therefore, a larger necessary r_d, decreasing the amount of measurements to be performed to cover the ROI and increase the viability of the method. However, this comes at the cost of lower SNR and a reduced resolution limit.

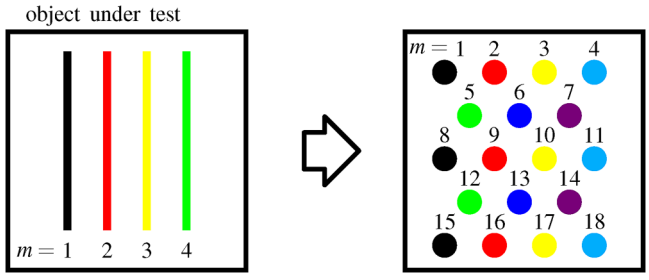

FIG. 3. Change in heating strategy to facilitate two-dimensional photothermal SR capabilities. In order to make achieving two-dimensional super resolution possible, the heating pattern needs to be two-dimensional as well. Therefore, a switch from line-wise to a point-wise step scanning on a measurement grid of equilateral triangles is proposed.

IV. NUMERICAL RECONSTRUCTION

The severely ill-posed fundamental equation of photothermal SR reconstruction as stated in Eq. (7) is formulated as a set of convolution problems $\Phi *_{x,y} a^m = T^m_{diff}$. Consequently, a suitable deconvolution algorithm needs to be applied to obtain a reconstruction of the internal heat source distribution a_{rec} and, therefore, of the inner defect structure of the OuT. For a similar problem in matrix vector product form $\Phi \cdot a^m = T^m_{diff}$, this can be achieved by applying the iterative convex optimization alternating direction method of multipliers (ADMM) algorithm[13] in conjunction with $\ell_{2,1}$-norm and ℓ_2-norm regularizing terms to constrain the solution

space,[14,15]

$$\underset{a_{\mathrm{rec}}}{\text{minimize}}: \quad 1/2\ \|\Phi\cdot a^m_{\mathrm{rec}} - T^m_{\mathrm{diff}}\|^2_2 + \lambda_{2,1}\|a^m_{\mathrm{rec}}\|_{2,1} + \lambda_2\|a^m_{\mathrm{rec}}\|^2_2, \tag{13}$$

where $\|a_{\mathrm{rec}}\|_{2,1}$ is the $\ell_{2,1}$-norm defined as

$$\|a_{\mathrm{rec}}\|_{2,1} = \sum_m \sqrt{\sum_{x,y} |a^m_{\mathrm{rec}}|^2}. \tag{14}$$

λ_2 and $\lambda_{2,1}$ are numerical weights controlling the strength of the regularizing terms in comparison to the least squares minimization term $1/2\|\Phi\cdot a^m_{\mathrm{rec}} - T^m_{\mathrm{diff}}\|^2_2$ and have to be empirically determined for optimal reconstruction results. Currently, it is part of an ongoing research, how to efficiently select the regularizer weights in the context of photothermal SR reconstruction using machine learning techniques.[16,17]

While the ℓ_2-norm constrains the amplitude of the reconstruction result, the $\ell_{2,1}$-norm incentivizes the reconstruction of (joint-) sparse defect/inhomogeneity structures, which effect multiple measurements. Since the defect/inhomogeneity structure of the OuT does not change for all measurements and defects/inhomogeneities are typically scarcely distributed within the ROI, this regularization approach greatly increases the reconstruction quality.

Additionally, the ADMM algorithm introduces a penalty parameter ρ (see detailed ADMM-implementations in Algorithms 1 and 2), which balances the effect of the least squares minimization term against the regularizing terms. This parameter can be determined programmatically using the L-curve method.[18]

Finally, the internal heat source distribution a_{int} widened by $I_{x,y}$ can be extracted by summing over all measurements where the external component a_{ext} is eliminated due to the homogeneity constraint as stated in Eq. (8),

$$n_m \times I_{x,y}(x,y) *_{x,y} a_{\mathrm{int}}(x,y) + const. = \sum_{m=1}^{n_m} a^m_{\mathrm{rec}}(x,y). \tag{15}$$

Furthermore, the constant term in Eq. (15) originating from Eq. (8) vanishes due the application of the ℓ_2-norm within the ADMM algorithm as it will converge to zero over the performed n_{iter} iterations.

Within Secs. IV A and IV B, two methods are proposed for transforming the spatial convolution problem into a multiplicative form, such that the aforementioned inversion via the ADMM algorithm can be performed.[19,20]

ALGORITHM 1. Sparse Matrix Stacking Reconstruction.

input : $H, T_{R0}, \rho, \lambda_{2,1}, \lambda_2, n_{\mathrm{iter}}$
output: a_{rec}
function $prox_{\ell_{21}+\ell_2}(l, \lambda_{2,1}, \lambda_2)$:
  $p[r,m] \leftarrow max\left(0, 1 - \frac{\lambda_{2,1}}{\sqrt{\sum_{m=1}^{n_m} |l[r,m]|^2}}\right)\frac{l[r,m]}{1+\lambda_2}$
  return p
$x^{(0)} \leftarrow \text{random\_uniform}_{[0,1[} \in \mathbb{R}^{n_x\cdot n_y\cdot n_m\times 1}$
$z^{(0)} \leftarrow \text{random\_uniform}_{[0,1[} \in \mathbb{R}^{n_x\cdot n_y\cdot n_m\times 1}$
$u^{(0)} \leftarrow x^{(0)} - z^{(0)}$
for k $\leftarrow$ 1 **to** n_{iter} **do**
  $x^{(k)} \leftarrow (H^T H + \rho I)^{-1}(H^T T_{R0} + \rho(A^{(k)} - u^{(k)}))$
  $l^{(k)} \leftarrow$ reshape $x^{(k)} + u^{(k-1)}$ **to** $\mathbb{R}^{n_x\cdot n_y\times n_m}$
  $p^{(k)} \leftarrow prox_{\ell_{21}+\ell_2}(l^{(k)}, \lambda_{2,1}/\rho, \lambda_2/\rho)$
  $z^{(k)} \leftarrow$ reshape $p^{(k)}$ **to** $\mathbb{R}^{n_x\cdot n_y\cdot n_m\times 1}$
  $u^{(k)} \leftarrow u^{(k-1)} - A^{(k)}$
end
$a_{\mathrm{rec}} \leftarrow \sum_{m=1}^{n_m}\left(\text{reshape } A^{(n_{\mathrm{iter}})} \textbf{ to } \mathbb{R}^{n_x\times n_y\times n_m}\right)$
return a_{rec}

A. Sparse matrix stacking

In order to transform the fundamental equation from a convolution problem into a multiplicative form to be able to use the ADMM algorithm for inversion, first the spatial dimensions have to be combined into one single dimension $r \in \{1, \ldots, n_x \cdot n_y\}$ by vectorizing,

$$\mathrm{vec}(\Phi \in \mathbb{R}^{n_x\times n_y}) = \Phi_r \in \mathbb{R}^{n_x\cdot n_y\times 1}, \tag{16}$$

$$\mathrm{vec}(a^m \in \mathbb{R}^{n_x\times n_y}) = a^m_r \in \mathbb{R}^{n_x\cdot n_y\times 1}, \tag{17}$$

$$\mathrm{vec}(T^m_{\mathrm{diff}} \in \mathbb{R}^{n_x\times n_y}) = T^m_r \in \mathbb{R}^{n_x\cdot n_y\times 1}. \tag{18}$$

After that, a convolution matrix operator $h(\cdot)$ can be introduced. This operator constructs for an input matrix of shape Φ_r a convolution matrix $h(\Phi_r) \in \mathbb{R}^{2n_x\cdot n_y - 1\times n_x\cdot n_y}$ such that

$$\Phi_r *_r a^m_r = T^m_{\mathrm{diff}} \quad \Leftrightarrow \quad h(\Phi_r)\cdot a^m_r = \begin{bmatrix} \underline{0} \\ T^m_r \\ \underline{0} \end{bmatrix} = T^m_{r0}. \tag{19}$$

Here, $T^m_{r0} \in \mathbb{R}^{2n_x\cdot n_y - 1}$ comprises the measured surface temperature data T^m_r symmetrically padded with $n_x \cdot n_y/2$ zeros. The convolution matrix $h(\Phi_r)$ constitutes a lower triangular matrix with Toeplitz-structure and is, therefore, quite sparsely populated. Since all n_m measurements need to be considered simultaneously for the reconstruction, the n_m equations can be stacked on top of each other as follows:

$$H\cdot A = \begin{bmatrix} \boxed{h} & & \underline{0} \\ & \boxed{h} & \\ \underline{0} & & \boxed{h} \end{bmatrix} \cdot \begin{bmatrix} a^1_r \\ \vdots \\ a^{n_m}_r \end{bmatrix} = \begin{bmatrix} T^1_{r0} \\ \vdots \\ T^{n_m}_{r0} \end{bmatrix} = T_{R0}, \tag{20}$$

with $h = h(\Phi_r)$, $H \in \mathbb{R}^{(2n_x\cdot n_y - 1)\cdot n_m \times n_x\cdot n_y\cdot n_m}$, $A \in \mathbb{R}^{n_x\cdot n_y\cdot n_m}$, and $T_{R0} \in \mathbb{R}^{(2n_x\cdot n_y - 1)\cdot n_m}$. Even though the dimensional size of the

ALGORITHM 2. Frequency Domain Reconstruction.

input : $\Phi_{\mathrm{PSF}}, T_{\mathrm{diff}}, \rho, \lambda_{2,1}, \lambda_2, n_{\mathrm{iter}}$
output: a_{rec}
function $prox_{\ell_{21}+\ell_2}(l, \lambda_{2,1}, \lambda_2)$:
  $p[i,j,m] \leftarrow max(0, 1 - \frac{\lambda_{2,1}}{\sqrt{\sum_{m=1}^{n_m} |l[i,j,m]|^2}}) \frac{l[i,j,m]}{1+\lambda_2}$
  return p

$A \leftarrow \mathrm{diag}\left(\text{reshape } \overline{\mathrm{fft}(\mathrm{ifftshift}(\Phi_{\mathrm{PSF}}))} \text{ to } \mathbb{R}^{n_x \cdot n_y \cdot n_m \times 1}\right)$
$b \leftarrow \text{reshape } \mathrm{fft}(T_{\mathrm{diff}}) \text{ to } \mathbb{R}^{n_x \cdot n_y \cdot n_m \times 1}$
$x^{(0)} \leftarrow \text{random\_uniform}_{[0,1[} \in \mathbb{R}^{n_x \cdot n_y \cdot n_m \times 1}$
$z^{(0)} \leftarrow \text{random\_uniform}_{[0,1[} \in \mathbb{R}^{n_x \cdot n_y \cdot n_m \times 1}$
$u^{(0)} \leftarrow x^{(0)} - z^{(0)}$
for k $\leftarrow$ 1 **to** n_{iter} **do**
  $x^{(k)} \leftarrow (A^T A + \rho I)^{-1}(A^T b + \rho(z - u))$
  $l^{(k)} \leftarrow \text{reshape } \mathrm{ifft}(x^{(k)} + u^{(k-1)}) \text{ to } \mathbb{R}^{n_x \times n_y \times n_m}$
  $p^{(k)} \leftarrow prox_{\ell_{21}+\ell_2}(l^{(k)}, \lambda_{2,1}/\rho, \lambda_2/\rho)$
  $z^{(k)} \leftarrow \text{reshape } \mathrm{fft}(p^{(k)}) \text{ to } \mathbb{R}^{n_x \cdot n_y \cdot n_m \times 1}$
  $u^{(k)} \leftarrow u^{(k-1)} - z^{(k)}$
end
$a_{\mathrm{rec}} \leftarrow \sum_{m=1}^{n_m} \left(\text{reshape } \mathrm{ifft}(z^{(n_{\mathrm{iter}})}) \text{ to } \mathbb{R}^{n_x \times n_y \times n_m}\right)$
return a_{rec}

matrix H is orders of magnitudes larger than the original data size of $n_x \cdot n_y \cdot n_m$ data points, it is as a diagonal matrix of sparse component matrices very sparse itself (only $\approx 1/2n_m$ of the entries in H contain a non-zero value), making it possible to be still efficiently stored and handled on modern computer hardware.

In summary, the following minimization problem emerged:

$$\underset{A}{\text{minimize}}: \quad 1/2 \; \|H \cdot A - T_{R0}\|_2^2 + \lambda_{2,1}\|A\|_{2,1} + \lambda_2 \|A\|_2^2 \qquad (21)$$

for which the algorithm presented as Algorithm 1 can be applied to solve for A and ultimately reconstruct the internal defect/inhomogeneity map as encoded in a_{int}.

The computational complexity of Algorithm 1 is mainly dominated by repeated matrix vector multiplications. Naïvely, this will run in at most $\mathcal{O}((2n_x \cdot n_y - 1)^2 \cdot n_x \cdot n_y \cdot n_m^3)$ time but due to the high degree of sparsity involved, this establishes only a very conservative upper bound.[21]

B. Minimization in the frequency domain

Another possible way to transform a spatial convolution problem into a multiplicative form is to switch into the spatial frequency domain. This can be achieved by means of a two-dimensional fast Fourier transform (FFT) as follows:

$$\Phi_{\mathrm{PSF}} *_{x,y} a^m \;\Leftrightarrow\; \mathrm{ifft}\left(\overline{\mathrm{fft}(\mathrm{ifftshift}(\Phi_{\mathrm{PSF}}))} \odot \mathrm{fft}(a^m)\right), \qquad (22)$$

where *fft* indicates the two-dimensional FFT in x and y, *ifft* its inverse, *ifftshift* a function that swaps the first quadrant with third and the second with the fourth quadrant of the input matrix, overlines designate taking the complex conjugate, and $\odot$ indicates element-wise multiplication (Hadamard product). In order to get rid of the element-wise multiplication and transform the problem to a matrix vector multiplication problem, the following substitution can be applied:

$$\mathrm{ifft}\left(\overline{\mathrm{fft}(\mathrm{ifftshift}(\Phi_{\mathrm{PSF}}))} \odot \mathrm{fft}(a)\right) \Leftrightarrow \mathrm{diag}\left(\mathrm{vec}\left(\overline{\mathrm{fft}(\mathrm{ifftshift}(\Phi_{\mathrm{PSF}}))}\right)\right) \cdot \mathrm{vec}(\mathrm{fft}(a)). \qquad (23)$$

Since the constraints governing the selection of the regularization terms for the problem inversion, like the sparse distribution of defects/inhomogeneities, are only applicable in the spatial domain, the problem has to be transformed back from the spatial frequency domain in order to apply their effect. This leads to one invocation of the *fft* and one of the *ifft* operation necessary per iteration.

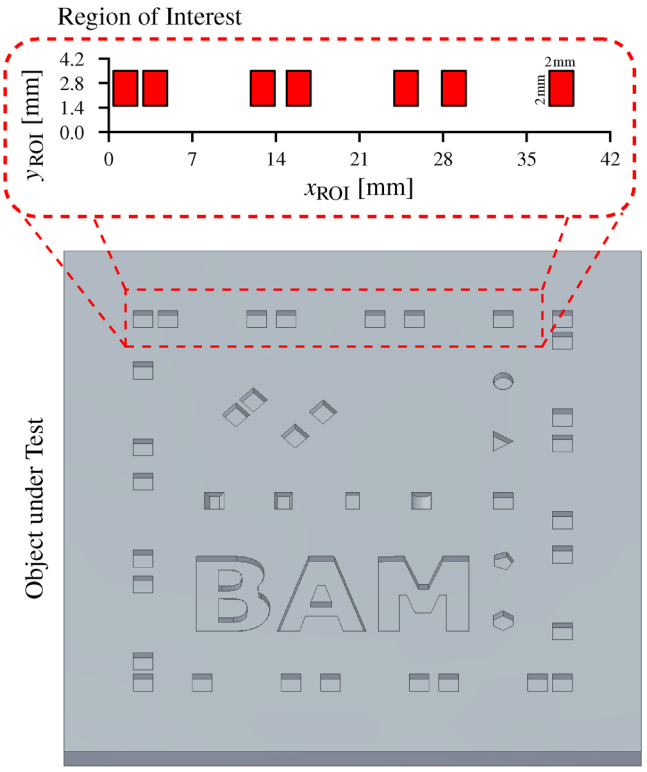

FIG. 4. Section view at a depth of $z = 1.5$ mm of the OuT: the OuT is additively manufactured from 316L stainless steel. The ROI for the experiment is marked as a dashed red box. A detailed map of the ROI with the locations of the defective regions shown as red boxes is overlayed on top. The cubical voids within the ROI have a side length of 2 mm and are fully covered by a defect-free 0.5 mm thick cover layer.

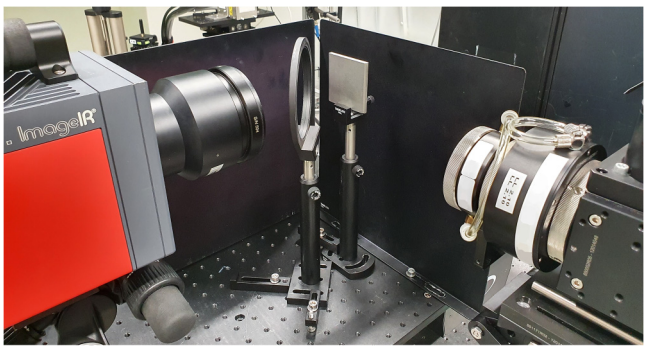

FIG. 5. Experimental setup: the OuT (middle) is heated by a fiber coupled diode laser with interchangeable projection objectives (right) and a maximum optical output power of $\hat{Q}_{max} = 500\,\mathrm{W}$ via a dichroitic mirror (middle). This mirror is highly reflective for the laser wavelength and transparent for midwave infrared radiation. The surface temperature is recorded with a midwave infrared camera with a detector size of $n_{pix} = 1280 \times 1024$ pixel at a spatial resolution of $\Delta x, \Delta y = 52\,\mu\mathrm{m}$ per pixel and a frame rate of $f_{cam} = 100\,\mathrm{Hz}$ (left). Scanning is achieved by utilizing two translational stages that move the OuT within the image plane of the laser focus objective.

The computational complexity of Algorithm 2 is mainly dominated by several invocations of the FFT per iteration. It will run in $\mathcal{O}(n_x \cdot n_y \cdot n_m \cdot \log(n_x \cdot n_y \cdot n_m))$ time, which is significantly less than the sparse matrix stacking minimization approach presented before for most circumstances.

V. EXPERIMENTAL SETUP

In order to test the experimental approach in conjunction with both proposed inversion algorithms as an extension to laser-based photothermal SR reconstruction, a purpose-made sample additively manufactured from 316L stainless steel has been examined. Within the ROI as shown in Fig. 4 lie multiple internal defects in the form of cubical voids with side length 2 mm, filled with unfused metal powder from the manufacturing process. The square OuT features a side length of 58.5 mm and a thickness of $L = 4.5\,\mathrm{mm}$, while its fused bulk material comes with a thermal conductivity of $k = 15\,\mathrm{W\,m^{-1}\,K}$, a density of $\rho = 7950\,\mathrm{kg\,m^{-3}}$, a specific heat capacity of $c_p = 502\,\mathrm{J\,kg^{-1}\,K^{-1}}$, and, therefore, an inferred thermal diffusivity of $\alpha = 3.76 \times 10^{-6}\,\mathrm{m^2\,s^{-1}}$.[22,23]

The ROI is chosen such that it covers several pairs of defects with a spacing of 0.5, 1, 2, and 4 mm between them. This allows not only for testing if all defects are detected by the algorithm but also if all defects can be detected as individual defects resulting in a measure of the resolution capabilities of the method.

As a photothermal heating source, a $\hat{Q}_{max} = 500\,\mathrm{W}$ fiber-couple diode laser with a wavelength of $\lambda = 940\,\mathrm{nm}$ is used. With this, the OuT front surface can be illuminated via reflecting off a dichroitic mirror (see Fig. 5), which is highly reflective for the laser wavelength but transparent for midwave infrared radiation. The surface temperature is subsequently measured with a midwave infrared camera with a detector size of $n_{pix} = 1280 \times 1024$ pixel at a spatial resolution of $\Delta x, \Delta y = 52\,\mu\mathrm{m}$ per pixel with a frame rate of $f_{cam} = 100\,\mathrm{Hz}$. Two linear translational stages are utilized to move the sample with respect to the laser and allow for scanning of the whole surface of the OuT.

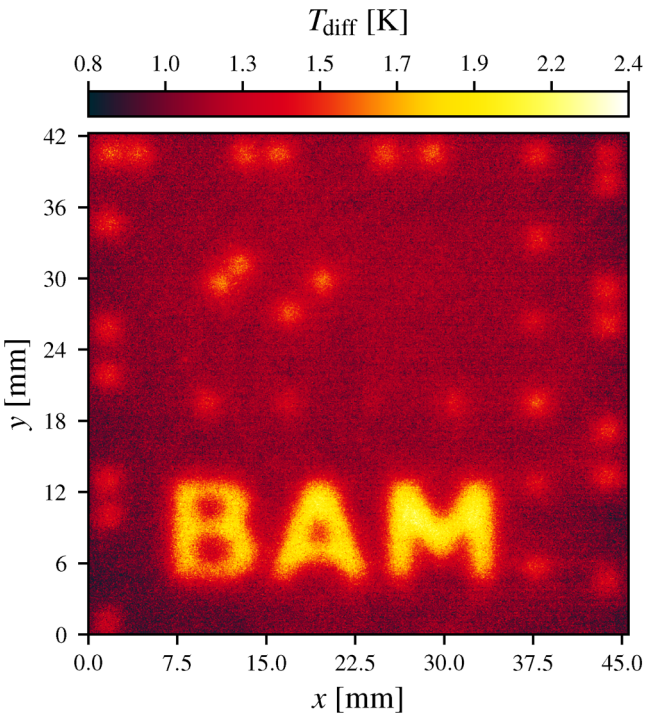

FIG. 6. Reference measurement for homogeneous illumination of the whole OuT surface with a laser pulse with $\hat{Q} = 500\,\mathrm{W}$ and a pulse length of $t_{pulse} = 500\,\mathrm{ms}$ evaluated at $t_{eval} = 500\,\mathrm{ms}$. For the generation of these data, the same setup as shown in Fig. 5 has been used.

VI. EXPERIMENTAL RESULTS

For a regular measurement grid of equilateral triangles of side length $r_d = 0.743\,\mathrm{mm}$ across the ROI with $n_m = 403$ vertices/independent measurement positions arranged in 7 rows with 54 or 53 positions each and subsequent reconstruction using the sparse matrix stacking approach, the resulting reconstruction of a_{rec} is shown in Fig. 7. At each grid point, a single measurement has been recorded after an illumination with a laser spot with spot size $d_{spot} = 0.6\,\mathrm{mm}$ at $\hat{Q} = 15\,\mathrm{W}$. To eliminate the time dimension, an evaluation time of $t_{eval} = 500\,\mathrm{ms}$ has been taken into account. This corresponds to a thermal diffusion length of $L_{diff} \approx 1.5\,\mathrm{mm}$.

The reconstruction result for applying the sparse matrix stacking algorithm is shown in Fig. 7. For this reconstruction, the ADMM-parameters $\lambda_{2,1} = 1570$, $\lambda_2 = 100$, $\rho = 16$, and $n_{iter} = 400$ have been used. As can be seen, all defects have been resolved as independent defects and the measurement noise has been successfully suppressed. The reconstruction of the exact defect geometry is still to be improved. For reference, in Fig. 6, the measured data for

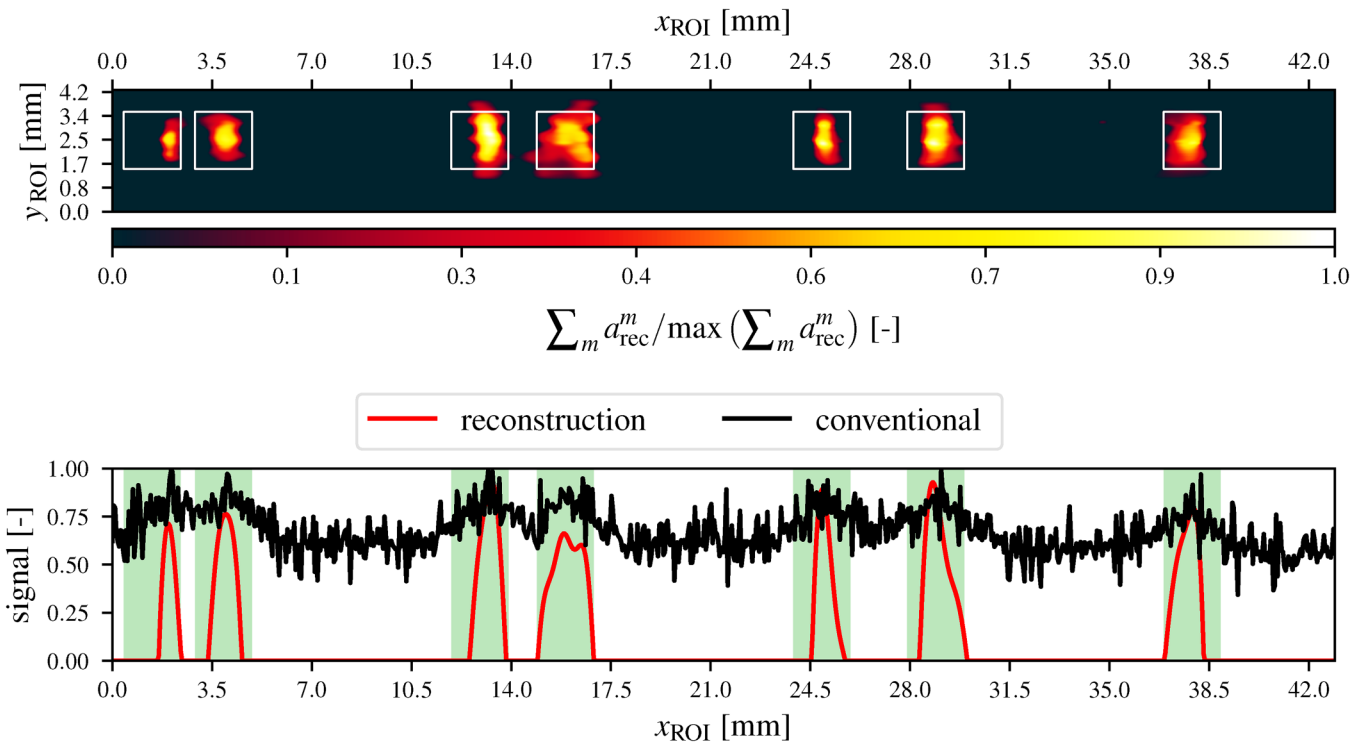

FIG. 7. Reconstruction result for a_{rec} at $t_{eval} = 500$ ms reconstructing using the sparse matrix stacking method. For this reconstruction, the ADMM-parameters $\lambda_{2,1} = 1570$, $\lambda_2 = 100$, $\rho = 16$, and $n_{iter} = 400$ have been used. The top figure shows a_{rec} with white boxes overlayed at the locations where the defective regions are. The bottom figure shows a sectional view of the data for $y_{ROI} = 2.5$ mm. The light green shaded areas mark the defective region. For reference, the normalized conventionally acquired data at the same coordinates from Fig. 6 are plotted as well.

illuminating the whole OuT front surface homogeneously using the same setup as for the point-wise illumination with $\hat{Q} = 500$ W and a pulse length of $t_{pulse} = 500$ ms are presented.

The reconstruction result for reconstructing a_{rec} within the spatial frequency domain is shown in Fig. 8. Here, the ADMM-parameters $\lambda_{2,1} = 27$, $\lambda_2 = 500$, $\rho = 16$, and $n_{iter} = 400$ have been used to achieve the shown reconstruction results. With reconstruction within the spatial frequency domain, a speedup of approximately 50 times has been found for the reconstruction within the given ROI, while this method is also much more sensitive to perturbation, making it harder to find a suitable set of parameters for the reconstruction.

In contrast to the sparse matrix stacking reconstruction result, this method also reconstructs the edges of the illuminated area as defects as can be seen near the left and right borders of the ROI. This can be explained by the local violation of the necessary condition for super resolution reconstruction given in Eq. (8). The sparse matrix stacking inversion method has been experienced to show much less dependence on the smoothness of the external excitation pattern. Even though both numerical inversion methods mathematically approximate the true solution to the same reconstruction problem, both methods show considerably different results. This can not only be explained due to performing the inversion either in the flattened spatial domain (sparse matrix stacking) or the spatial frequency domain (FFT-based method) but also by the high non-linearity and filtering properties of the used solver in form of the ADMM algorithm and the applied regularizing terms. How to exploit those differences to improve the reconstruction quality is still part of an ongoing research.

In order to better assess the resolution gain of the proposed photothermal SR reconstruction methods compared to well-established conventional methods, a qualitative comparison of different methods can be found in Fig. 9. Here, the reconstruction results of both proposed photothermal SR reconstruction methods is shown next to raw data acquired after homogeneous illumination (cf. Fig. 6) as-is and after different post-processing steps. The homogeneous illumination data are recorded within the same setup as shown in Fig. 5. The additional post-processing steps shown contain a difference thermogram where from the measured raw data T_{diff}, the temperature evolution of a region of the same OuT without defects is subtracted. As a second post-processing method, the amplitude and phase data for a pulsed phase thermography (PPT) of T_{diff} for an evaluation frequency of $f_{PPT} = 0.1$ Hz (found to feature the highest contrast for this dataset) are shown.[24]

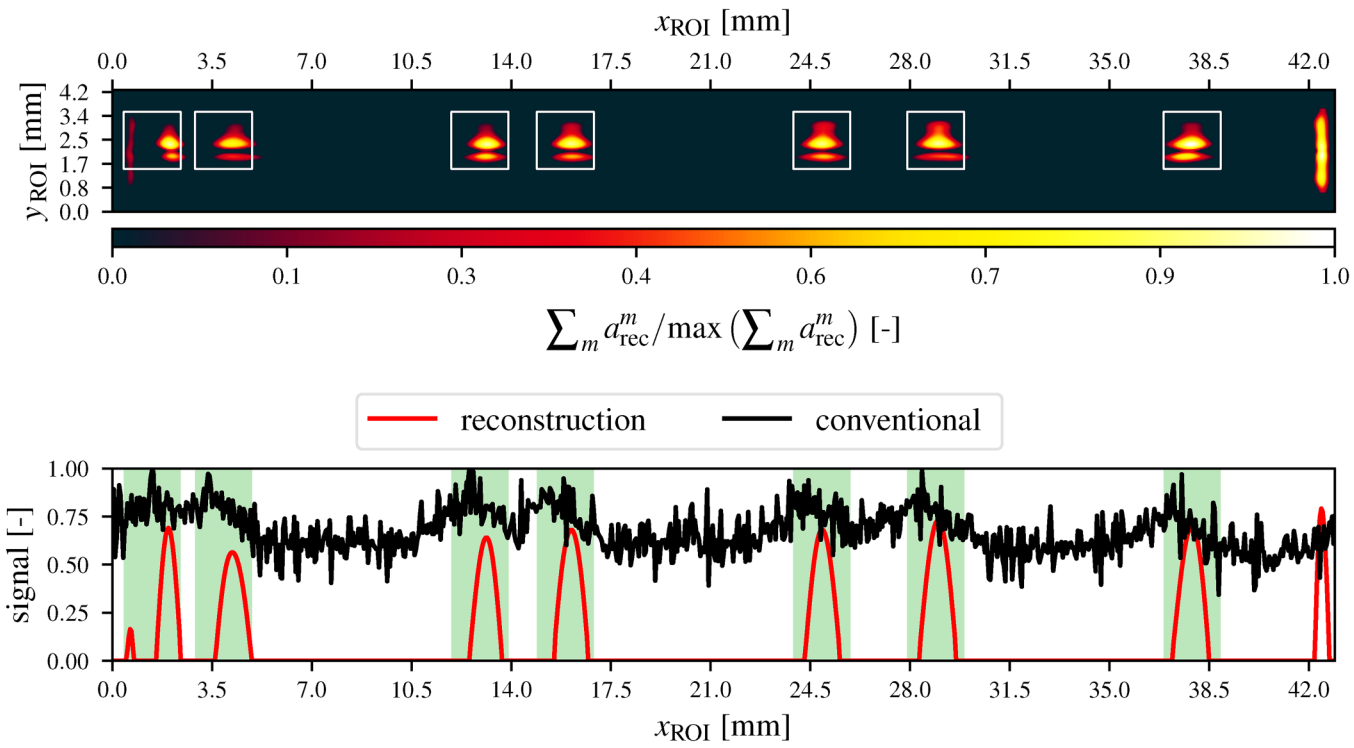

FIG. 8. Reconstruction result for a_{rec} at $t_{eval} = 700$ ms reconstructing within the frequency domain. For this reconstruction, the ADMM-parameters $\lambda_{2,1} = 27$, $\lambda_2 = 500$, $\rho = 16$, and $n_{iter} = 400$ have been used. The top figure shows a_{rec} with white boxes overlayed at the locations where the defective regions are. The bottom figure shows a sectional view of the data for $y_{ROI} = 1.92$ mm. The light green shaded areas mark the defective region. For reference, the normalized conventionally acquired data at the same coordinates from Fig. 6 are plotted as well.

Since quantitatively comparing the increase in resolution capability comparing the sparse reconstruction results gained from photothermal SR reconstruction and dense measurement data acquired from conventional methods is not trivially possible, we limit ourselves to a qualitative comparison only where our main criterion comprises the separability of closely spaced defects by the method. As can be seen in Fig. 9, in the difference thermogram, as well as a PPT analysis of T_{diff}, all defects are detected, but the smallest gap between defects ($d_{gap} = 0.5$ mm) cannot be clearly identified with the available SNR of the measurement. In this direct comparison, the advantage of the sparse nature of the reconstruction of the photothermal SR reconstruction results can be clearly identified. Here, all defects can be clearly separated.

VII. CONCLUSION AND OUTLOOK

Within this work, an experimental approach for expanding the capabilities of laser-based photothermal SR reconstruction to the detection of two-dimensional defects has been successfully introduced. Two numerical inversion methods for the reconstruction of the internal defect/inhomogeneity structure of an OuT have been proposed and their reconstruction performance has been tested experimentally. Both proposed numerical methods have proven to make it possible to detect even closely positioned defects individually and both methods have provided an approximation of the defect shape. While the proposed sparse matrix stacking inversion method led to qualitatively better shape reconstruction, it took almost 50 times more time to compute on modern computer hardware, making it less suited for the reconstruction of large ROIs. The reconstruction in the frequency domain has proven to be more sensitive to the choice of regularization parameters and to imperfections in the measurements but takes less time to compute and is more memory efficient. Both methods are still equally affected by the lack of a suitable method for finding the best suited set weights for the regularizing terms programmatically in a feasible amount of time. Solving this issue and the improvement of the reconstruction quality of the defect shape is still part of an ongoing research.[16]

As the presented experimental approach can be recreated using pre-existing standard equipment, a simple adaptation for existing industrial test processes is possible. Its capability of achieving super resolution further allows for the detection of defects beyond the spatial resolution limit of the conventional methods presented. In addition, the sparse nature of the reconstruction results highly contrasts defective regions and allows for easy automation of the test result evaluation process. However, the experimental prerequisite to perform a large amount of sequential

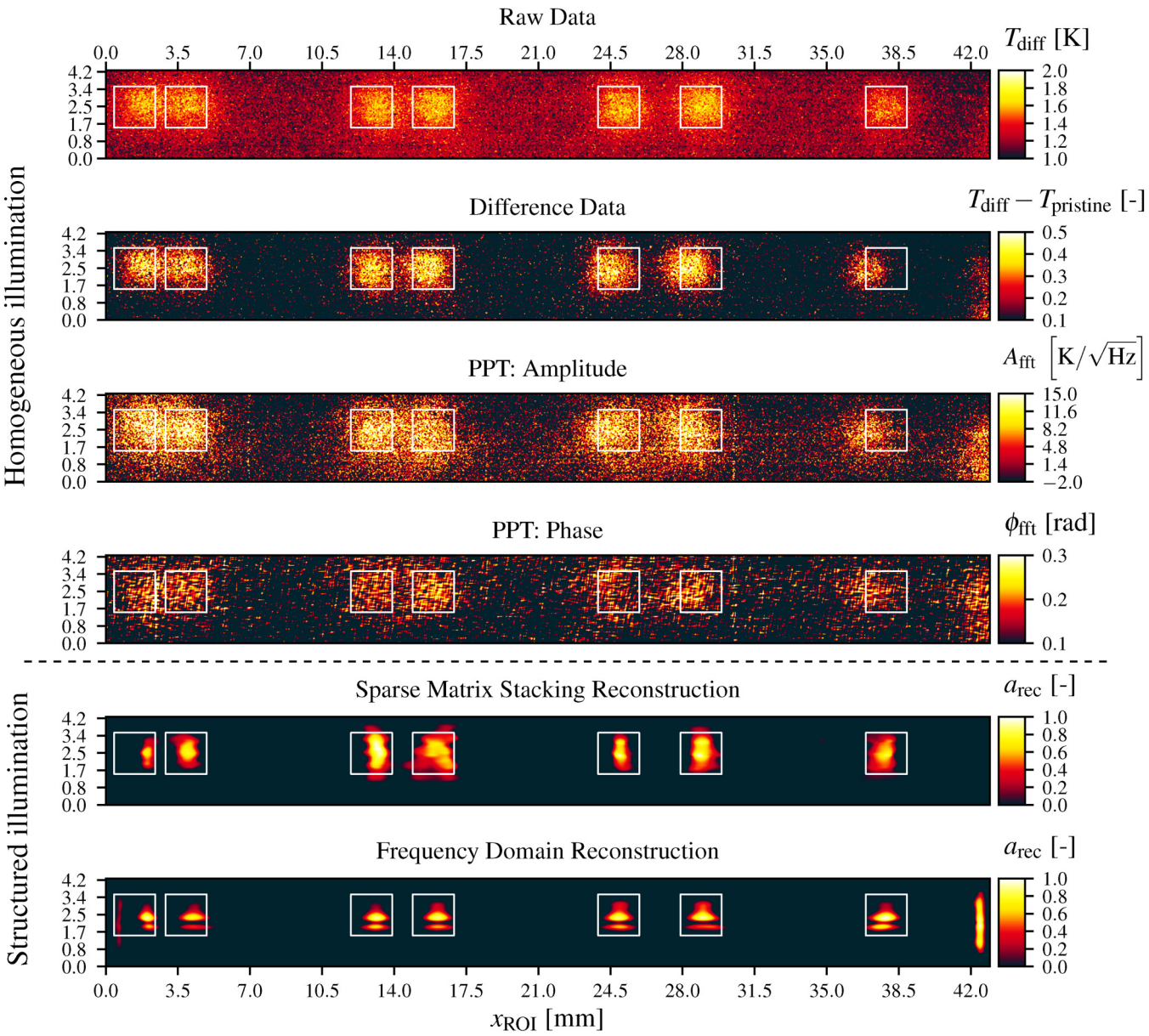

FIG. 9. Defect detection performance comparison of the proposed photothermal SR reconstruction methods with conventional methods. From top to bottom: unprocessed measured data T_{diff} from Fig. 6 for the chosen ROI; difference thermogram showing the difference of the measured data and the measurement data for a different defect-free ROI; frequency amplitude data for a frequency of $f_{\mathrm{PPT}} = 0.1$ Hz for T_{diff} processed by PPT; frequency phase data for a frequency of $f_{\mathrm{PPT}} = 0.1$ Hz for T_{diff} processed by PPT; a_{rec} as reconstructed by photothermal SR reconstruction with the proposed sparse matrix stacking method; a_{rec} as reconstructed by photothermal SR reconstruction in the frequency domain. The white boxes in each plot indicate the true defect positions.

independent measurements with single laser-spot excitation to cover larger ROIs is still to be improved for this method. While for testing scenarios demanding high-defect detection resolution at larger depths, the increased testing effort can be justified, e.g., for high-performance parts for aerospace applications or for medical diagnostics, for high-volume/low-cost testing scenarios, the experimental complexity still needs to be improved. Here, the projection of two-dimensional pixel patterns using the latest laser-projector technology shows promising results to significantly reduce the necessary number of measurements.[25]

AUTHOR DECLARATIONS

Conflict of Interest

The authors have no conflicts to disclose.

DATA AVAILABILITY

The data that support the findings of this study are available from the corresponding author upon reasonable request.

REFERENCES

[1]M. S. Alam, J. G. Bognar, R. C. Hardie, and B. J. Yasuda, "Infrared image registration and high-resolution reconstruction using multiple translationally shifted aliased video frames," IEEE Trans. Instrum. Meas. **49**, 915–923 (2000).

[2]E. Mandanici, L. Tavasci, F. Corsini, and S. Gandolfi, "A multi-image super-resolution algorithm applied to thermal imagery," Appl. Geomatics **11**, 215–228 (2019).

[3]E. A. Ingerman, R. A. London, R. Heintzmann, and M. G. L. Gustafsson, "Signal, noise and resolution in linear and nonlinear structured-illumination microscopy," J. Microsc. **273**, 3–25 (2018).

[4]B.-K. Wang, M. Barbiero, Q. Zhang, and M. Gu, "Super-resolution optical microscope: Principle, instrumentation, and application," Front. Inf. Technol. Electron. Eng. **20**, 608–630 (2019).

[5]S. Ahmadi, P. Burgholzer, G. Mayr, P. Jung, G. Caire, and M. Ziegler, "Photothermal super resolution imaging: A comparison of different thermographic reconstruction techniques," NDT & E Int. **111**, 102228 (2020).

[6]S. Ahmadi, J. Lecompagnon, P. D. Hirsch, P. Burgholzer, P. Jung, G. Caire, and M. Ziegler, "Laser excited super resolution thermal imaging for nondestructive inspection of internal defects," Sci. Rep. **10**, 436 (2020).

[7]P. Burgholzer, M. Haltmeier, T. Berer, E. Leiss-Holzinger, and T. W. Murray, *Super-Resolution Photoacoustic Microscopy Using Joint Sparsity* (Optical Society of America, 2017).

[8]P. Burgholzer, T. Berer, J. Gruber, and G. Mayr, "Super-resolution thermographic imaging using blind structured illumination," Appl. Phys. Lett. **111**, 031908 (2017).

[9]S. Kaiplavil and A. Mandelis, "Truncated-correlation photothermal coherence tomography for deep subsurface analysis," Nat. Photonics **8**, 635–642 (2014).

[10]P. Tavakolian, K. Sivagurunathan, and A. Mandelis, "Enhanced truncated-correlation photothermal coherence tomography with application to deep subsurface defect imaging and 3-dimensional reconstructions," J. Appl. Phys. **122**, 023103 (2017).

[11]K. Cole, J. Beck, A. Haji-Sheikh, and B. Litkouhi, *Heat Conduction Using Greens Functions* (CRC Press, 2010).

[12]S. Ahmadi, G. Thummerer, S. Breitwieser, G. Mayr, J. Lecompagnon, P. Burgholzer, P. Jung, G. Caire, and M. Ziegler, "Multidimensional reconstruction of internal defects in additively manufactured steel using photothermal super resolution combined with virtual wave-based image processing," IEEE Trans. Ind. Inf. **17**, 7368–7378 (2021).

[13]S. Boyd, "Distributed optimization and statistical learning via the alternating direction method of multipliers," Found. Trends Mach. Learn. **3**, 1–122 (2010).

[14]M. Haltmeier, T. Berer, S. Moon, and P. Burgholzer, "Compressed sensing and sparsity in photoacoustic tomography," J. Opt. **18**, 114004 (2016).

[15]Y. Yu, "On decomposing the proximal map," in *Proceedings of the 26th International Conference on Neural Information Processing Systems*, NIPS'13 (Curran Associates Inc., Red Hook, 2013), Vol. 1, pp. 91–99.

[16]S. Ahmadi, J. C. Hauffen, L. Kästner, P. Jung, G. Caire, and M. Ziegler, "Learned block iterative shrinkage thresholding algorithm for photothermal super resolution imaging," arXiv:http://arxiv.org/abs/2012.03547v2[cs.CV] (2020).

[17]S. Ahmadi, L. Kästner, J. C. Hauffen, P. Jung, and M. Ziegler, "Photothermal-SR-Net: A customized deep unfolding neural network for photothermal super resolution imaging," arXiv:2104.10563[cs.CV] (2021).

[18]P. C. Hansen, "Regularization tools: A Matlab package for analysis and solution of discrete ill-posed problems," Numer. Algorithms **6**, 1–35 (1994).

[19]J. Lecompagnon, S. Ahmadi, P. Hirsch, and M. Ziegler, "Full-frame thermographic super-resolution with 2D-structured laser heating," in *Thermosense: Thermal Infrared Applications XLIII*, International Society for Optics and Photonics Vol. 11743, edited by J. N. Zalameda and A. Mendioroz (SPIE, 2021), pp. 200–208.

[20]J. Lecompagnon, S. Ahmadi, P. D. Hirsch, and M. Ziegler, "2D-Photothermal super resolution with sparse matrix stacking," in *SMSI 2021—Sensors and Instrumentation, Satellite Conference: Infrared Sensor Applications: Non-destructive Testing, Spectroscopy* (AMA Service GmbH, Wunstorf, 2021), Chap. C2 IRS^2, pp. 183–184.

[21]R. Yuster and U. Zwick, "Fast sparse matrix multiplication," ACM Trans. Algorithms **1**, 2–13 (2005).

[22]Erpro Group—SAS, "Material data sheet stainless steel 316L/1.4404/A276," (2019), see https://erpro-group.com/wp-content/uploads/2019/04/Fe_316L.pdf.

[23]ASM International, *Materials and Coatings for Medical Devices: Cardiovascular* (ASM International, Materials Park, OH, 2009), p. 135.

[24]C. Ibarra-Castanedo and X. Maldague, "Pulsed phase thermography reviewed," Quant. Infrared Thermogr. J. **1**, 47–70 (2004).

[25]J. Lecompagnon, S. Ahmadi, P. Hirsch, C. Rupprecht, and M. Ziegler, "Investigations on photothermal super resolution reconstruction using 2D-structured illumination patterns," in *SPIE Future Sensing Technologies 2021*, edited by C. R. Valenta, J. A. Shaw, and M. Kimata (SPIE, 2021).